OPTICS

Synchrotron radiation from an accelerating light pulse

M. Henstridge[1,2], C. Pfeiffer[1,3], D. Wang[1,4], A. Boltasseva[1,4], V. M. Shalaev[1,4], A. Grbic[1,3], R. Merlin[1,2]*

Synchrotron radiation—namely, electromagnetic radiation produced by charges moving in a curved path—is regularly generated at large-scale facilities where giga–electron volt electrons move along kilometer-long circular paths. We use a metasurface to bend light and demonstrate synchrotron radiation produced by a subpicosecond pulse, which moves along a circular arc of radius 100 micrometers inside a nonlinear crystal. The emitted radiation, in the terahertz frequency range, results from the nonlinear polarization induced by the pulse. The generation of synchrotron radiation from a pulse revolving about a circular trajectory holds promise for the development of on-chip terahertz sources.

Synchrotron radiation (that is, the emission from a relativistic charge moving along a circular trajectory) was first observed in 1947 (*1*). Until the 1960s, synchrotrons were used to accelerate charged particles exclusively for experiments in particle physics, and radiation losses were studied primarily because they were an impediment to achieving high energies (*2*–*4*). Presently, large-scale synchrotrons that produce high-intensity x-rays are used in a wide range of scientific studies. Synchrotron radiation has also been produced at radio frequencies from accelerating polarization currents created by capacitor arrays (*5*) and is commonly observed in astrophysical phenomena such as radio galaxies and supernovae (*6*).

Here we present the observation of synchrotron radiation resulting from the acceleration of a light pulse (*7*–*11*). Our work distinguishes itself from previous studies involving accelerated beams in nonlinear media (*12*–*14*) in that the emphasis is placed on the identification of features exclusively associated with the centripetal acceleration of the primary beam. A metasurface (*15*–*20*) was used to guide a pulse of 800-nm central wavelength and 100-fs duration along a 100-μm–scale circular arc inside a lithium tantalate ($LiTaO_3$) crystal. As the pulse mixes with itself through the second-order susceptibility of the crystal, the accelerating light pulse generates both second-harmonic and difference-frequency nonlinear polarizations. As for a charge moving under the influence of a centripetal force in vacuum, interference effects lead to a nonlinear polarization, which moves along a circular path and emits synchrotron radiation, as if acted upon a fictitious force (*21*). We measure the emission from the difference-frequency polarization, which is in the terahertz range, over a scale of 100 μm.

In $LiTaO_3$, the nonlinear polarization generated by a 800-nm pulse propagates at approximately three times the phase velocity of light at terahertz frequencies, below those of the lowest-lying transverse optical (TO) phonons of A_1 and E symmetry (*22*). As a result, synchrotron radiation at these frequencies interweaves strongly with Cherenkov radiation (*23*–*26*), and as such, its spectrum has features that are fundamentally different from those of charges circulating at subluminal speeds. Because the polarization field defines the local dipole density, the general properties of the radiation produced by our pulses relate to those of emission resulting from the motion of a single dipole or, more simply, from a charge q that moves at a constant speed v about a circular path. Assuming that the charge makes an infinite number of revolutions, the power emitted into the mth harmonic of the revolution frequency, $\omega_0 = v/R$, is given by (*26*)

$$P_m = \frac{q^2 v m \omega_0^2}{c^2}\left[2J'_{2m}(u) + (1 - c^2/n^2v^2)\int_0^u J_{2m}(x)dx\right] \quad (1)$$

where R is the radius of the circle; J_{2m} and J'_{2m} are, respectively, the Bessel function of order $2m$ and its derivative; c is the speed of light in vacuum; n is the index of refraction at the mth harmonic and $u = 2mvn/c$. This expression is valid both for $v < c/n$ and $v > c/n$. For light polarized parallel to the optical axis of $LiTaO_3$, $n = 6.3$ at frequencies considerably below that of the lowest-lying A_1-type TO phonon, at 6.0 THz (*22*), whereas the group index at 800 nm is $n_g = 2.2$ (*27*). Figure 1 shows the calculated discrete power spectra for emission from a charge at both subluminal and superluminal speeds in a medium with constant $n = 6.3$. The radiated power increases with frequency when $v > c/n$, whereas for $v < c/n$, the emission spectrum exhibits a cutoff at a critical frequency $\omega_C = 3\omega_0/2(1 - v^2n^2/c^2)^{3/2}$ beyond which the radiation emitted is negligible (this is more clearly seen on a linear scale) (*28*). In our experiments, the highest synchrotron frequency attainable is determined by the bandwidth of the pump

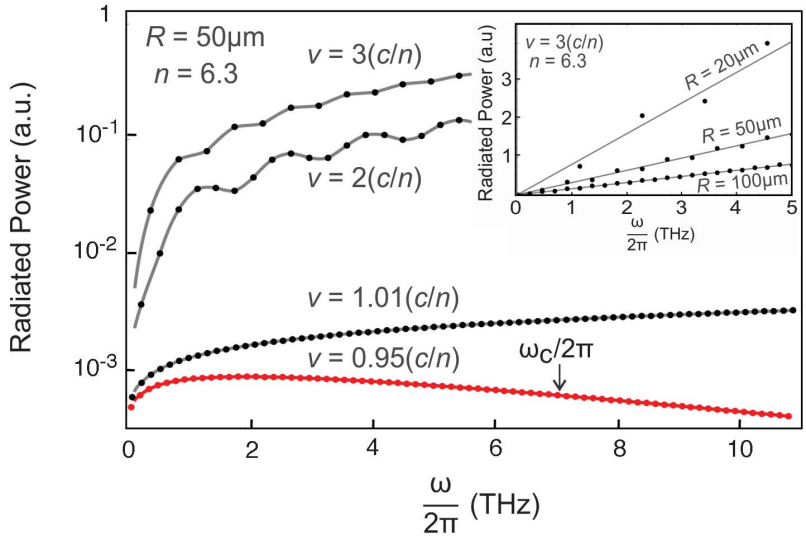

Fig. 1. Radiated power: Comparison between subluminal and superluminal speeds. Calculated power radiated by a charge moving in a circle of radius $R = 50$ μm, at speeds below and above c/n, in a medium with constant $n = 6.3$ (note the logarithmic scale) is shown. Emission is at integer multiples of the fundamental frequency $\omega_0 = v/r$. At subluminal speeds, the emitted power drops rapidly for frequencies greater than the critical angular frequency ω_C. (**Inset**) Results for $v = 3c/n$ and three different radii (linear scale). For speeds $v >> c/n$, the power emitted into harmonics behaves linearly with slope given by $(q^2v/c^2)(1 - c^2/v^2n^2)\omega_0$. The curves and lines are guides for the eye. a.u., arbitrary units.

[1]Center for Photonics and Multiscale Nanomaterials, University of Michigan, Ann Arbor, 48109, USA. [2]Department of Physics, University of Michigan, Ann Arbor, MI 48109, USA. [3]Department of Electrical Engineering and Computer Science, University of Michigan, Ann Arbor, MI 48109, USA. [4]School of Electrical and Computer Engineering and Birck Nanotechnology Center, Purdue University, West Lafayette, IN 47907, USA.
*Corresponding author. Email: merlin@umich.edu

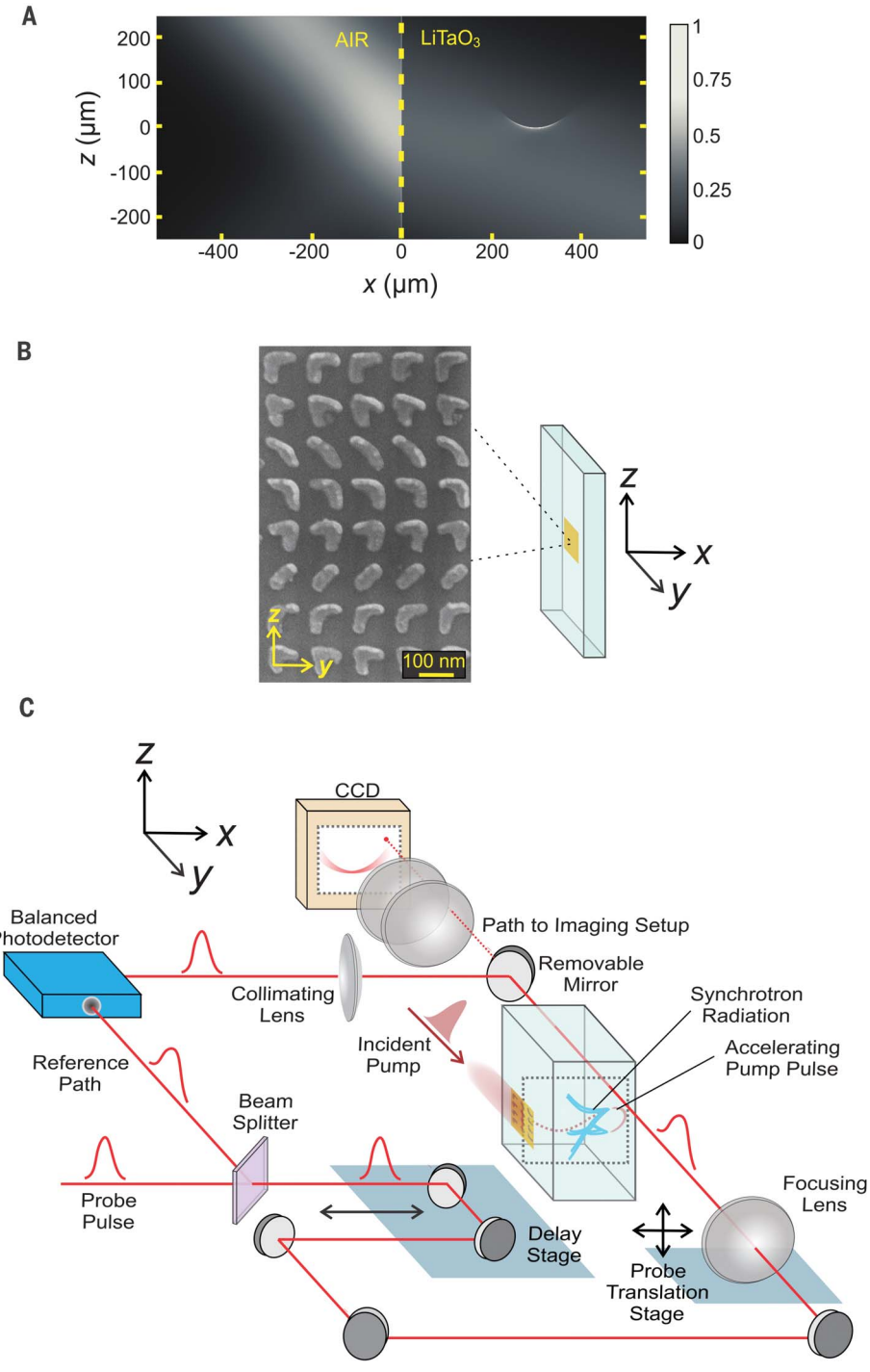

Fig. 2. Accelerated beam, metasurface, and experimental setup. (**A**) Two-dimensional plot showing the intensity of the incident and elastically scattered field from the metasurface, located at $x = 0$. The reflected beam intensity is roughly five times smaller than that of the incident beam. (**B**) Scanning electron microscope image of a section of the nanoantenna array fabricated onto the $LiTaO_3$ substrate. To facilitate the imaging of the accelerating beam, the leading edge of the metasurface was positioned ≈1 mm away from the edge of the substrate. The array was aligned to obtain an accelerating beam in the *xz* plane, in accordance with the 2D plot shown in (A). The pattern repeats periodically along the *y* axis; the width of the accelerating beam parallel to this axis is determined by the width of the incident beam. (**C**) Schematic of the orthogonal pump-probe setup. The output of a measurement set is an image sequence showing the time evolution of the time derivative of the pump-pulse intensity and the terahertz synchrotron radiation field. The dotted curve inside the crystal denotes the trajectory of the accelerating pump pulse. CCD, charge-coupled device.

pulses. For speeds considerably greater than c/n, the radiated power increases substantially. For example, the power radiated at a given frequency for $v = 3c/n$ is several orders of magnitude larger than that at a nearby frequency for $v = 0.95c/n$. We emphasize the facts that these results assume a frequency-independent refractive index and that the spectra consist of discrete lines only if the motion is strictly periodic; a source undergoing a few cycles or a fraction of a cycle emits instead a continuous spectrum. This applies to conventional synchrotron radiation for which the source is a single charge, as well as to a nonlinear polarization moving along a circular path.

Calculated spectra for an electron revolving in a medium with constant $n = 6.3$ and $v = 3c/n$ for three different radii are shown in the inset of Fig. 1. The values for the electron velocity and light speed are similar to those in our experiments on $LiTaO_3$. The fact that the radiation involves a few discrete frequencies suggests that light-produced synchrotron terahertz radiation could be useful as a means to obtain on-chip continuous-wave terahertz sources. Furthermore, synchrotron emission from a nonlinear accelerating polarization can serve as a new method for generating coherent light at any frequency and in any medium at which conventional phase-matching with the nonlinear polarization is poor, such as at frequencies immediately above the Reststrahlen band in crystals such as ZnTe or GaP, or at second-harmonic frequencies. Within this context, we note a report of unusually phase-matched second-harmonic generation using Bessel beams (*29*).

We designed a plasmonic nanoantenna metasurface (*17*, *18*) to accelerate light of wavelength 800 nm along a circular arc of radius of curvature equal to 100 μm, inside the $LiTaO_3$ crystal. Unlike conventional methods for accelerating light, which rely on spatial light modulators (*30*), metasurfaces have the ability to bend light at arbitrarily large angles from the normal to a planar interface and thereby produce trajectories of very small radii inside a material (*31*). The nanoantennas scatter roughly 5% of the incident power into the accelerating beam, which is cross-polarized relative to the incident polarization. Approximately 50% of the incident beam power is transmitted unperturbed and ~20% is reflected. To reduce the spatial overlap between the unperturbed and accelerating beams, the nanoantennas were arranged to produce an accelerating beam when illuminated at a 45° angle of incidence. The design process is described in detail in (*31*) and summarized in the supplementary materials (*32*). A two-dimensional (2D) plot showing the calculated incident and scattered intensities for continuous-wave illumination at 800 nm is shown in Fig. 2A. Calculations of the accelerating pulse produced by the metasurface when illuminated with a pulse from an ultrafast laser are presented in (*32*).

The 500-μm–by–500-μm metasurface was fabricated onto a 1-mm-thick $LiTaO_3$ substrate by using electron-beam lithography and lift-off techniques. Prior to fabrication, all four of the 1-mm-wide sides of the substrate were polished to optical quality to eliminate Rayleigh scattering. Details are discussed in (*32*). A schematic describing the positioning of the metasurface and a scanning electron microscope image of the nanoantennas are shown in Fig. 2B.

The accelerating pulse was generated by illuminating the metasurface with a pulse of 800-nm central wavelength and duration of 100 fs from a regeneratively amplified Ti:sapphire oscillator operating at the repetition rate of 250 kHz. We performed a spatially resolved pump-probe experiment in the differential transmission geometry to detect the terahertz radiation generated by the accelerating pulse. The experimental setup is shown in Fig. 2C. The probe pulse is polarized parallel to the optical (z) axis while the electric field of the accelerating pump lies in the xz plane and rotates slightly as the pulse propagates. The component of the nonlinear polarization, $\mathbf{P}_{NL}$, relevant to our experiments is that along the optical axis $\mathbf{P}_{NL}.\hat{z} = \chi^{(2)}_{333}|\mathbf{E}_P.\hat{z}|^2$; here, $\mathbf{E}_P$ is the field of the pump, and $\chi^{(2)}_{333}$ is the corresponding element of the second-order nonlinear susceptibility. The probe beam directed to the sample was focused to a spot with a full width at half maximum (FWHM) of 10 μm in the plane of the accelerating beam trajectory. The probe's focusing lens was mounted onto a motorized translation stage, allowing for the translation of the focal spot throughout the acceleration plane. To calibrate the position of the probe, the accelerating and focused probe beams were first imaged together using a standard imaging setup. The transmitted probe was then directed to a balanced photodetector at which its average intensity was subtracted from that of the reference beam. The focal spot was translated throughout a 400-μm–by–400-μm area of the accelerating beam plane in steps of 10 μm. At each position, the arrival time of the probe pulse was delayed in steps of 53.4 fs, and the corresponding differential intensity trace was recorded. The output of a completed measurement is an image sequence showing the propagation of the time-derivatives of the 800-nm pump-pulse intensity and terahertz synchrotron field. We did not measure the power spectrum of the terahertz radiation. As noted earlier and as opposed to the discrete emission resulting from repeated rotations (Fig. 1), we expect it to be a continuum because the accelerating pulse moves just a fraction of one cycle. Further details concerning the experiment and the processing of the data are presented in the supplementary materials (*32*).

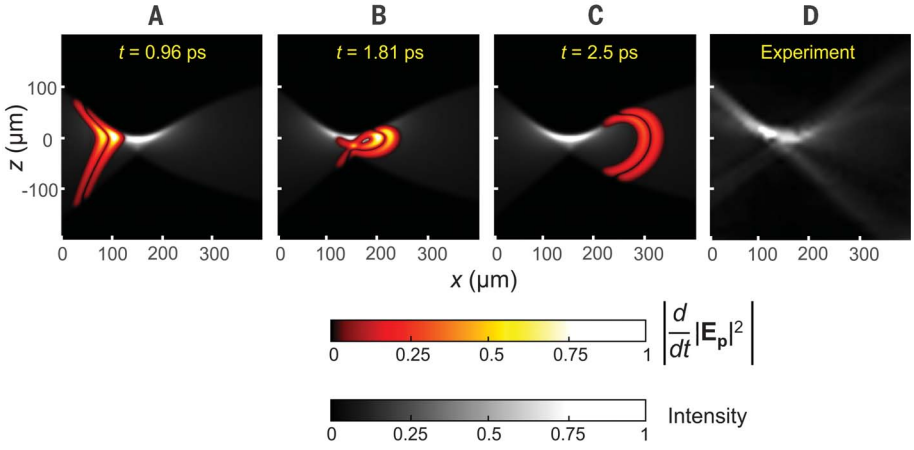

Fig. 3. Accelerating pump pulse. (**A** to **C**) Two-dimensional plots showing the calculated magnitude of the time derivative of the pump-pulse intensity, $|\mathbf{E}_P|^2$, and the intensity for continuous-wave excitation at 800 nm. To compare with the experimental data, results were numerically convolved with a Gaussian function with 10-μm FWHM. (**D**) Image of the accelerating beam trajectory obtained by adding the series of experimental traces for $|d|\mathbf{E}_P|^2/dt|$.

Figure 3 displays calculated 2D plots of the accelerating pump pulse alone, at different positions along the beam trajectory, as well as an experimental image of the accelerating beam trajectory obtained from the pump-probe measurements. The main results of this work are presented in Fig. 4. Panels A to D show plots of the measured time derivatives of the terahertz electric field and pump intensity for four different arrival times of the probe. In all cases, the unperturbed incident pulse, which passes through the metasurface, was digitally removed. Consistent with results reported in (*33*), this pulse generates a negligible amount of terahertz radiation at its edges, which was also removed from the data. Panels E to H of Fig. 4 show the corresponding theoretical simulations. For comparison purposes, results of calculations for the radiation emitted by a single dipole are displayed in panels I to L.

The theoretical difference-frequency synchrotron electric field was obtained by numerically solving the following scalar, inhomogeneous wave equation for each terahertz frequency component

$$\left(\frac{\partial^2}{\partial x^2}+\frac{\partial^2}{\partial z^2}+\frac{\Omega^2}{c^2}\varepsilon(\Omega)\right)E_S = \frac{1}{c^2}\frac{\partial^2 P_{NL}}{\partial t^2}\bigg|_\Omega \approx \frac{1}{c^2}\frac{\partial^2}{\partial t^2}\left(\chi^{(2)}_{333}|\mathbf{E}_P|^2\right)\bigg|_\Omega \quad (2)$$

Here, Ω is the terahertz frequency and $f(t)|_\Omega$ denotes the Fourier transform of $f(t)$ at Ω. E_S (x, z, Ω) and P_{NL} are the z component of, respectively, the synchrotron electric field and the nonlinear polarization; $\mathbf{E}_P$ is the electric field of the 800-nm accelerating pump pulse; and $\varepsilon(\Omega)$ is the far-infrared permittivity of $LiTaO_3$ for radiation polarized parallel to the optical axis (*32*). For simplicity, we assumed that the polarization of the electric field is normal to the accelerating beam trajectory; that is, we ignored effects due to the rotation of the accelerating pump polarization. The theoretical plots in Fig. 4, E to H, were generated by taking the time derivatives of the solution to Eq. 2 and the calculated accelerating pulse intensity. The 2D matrix for each plot was then convolved with a Gaussian function of 10-μm FWHM to account for the size of the probe's focal spot. The complete image sequence showing the time evolution of the pump pulse and synchrotron field is presented in (*32*).

The simulations reproduce most of the features observed in the experiments, and there is reasonably good quantitative agreement between the two sets of results shown, respectively, in panels E to H and A to D of Fig. 4. Consistent with the optical properties of $LiTaO_3$, the 800-nm pulse propagates at a speed approximately three times that for the terahertz synchrotron field. As mentioned earlier, the superluminal nature of the propagation leads to new features in the radiation pattern, which distinguish themselves from those of ordinary, subluminal synchrotron

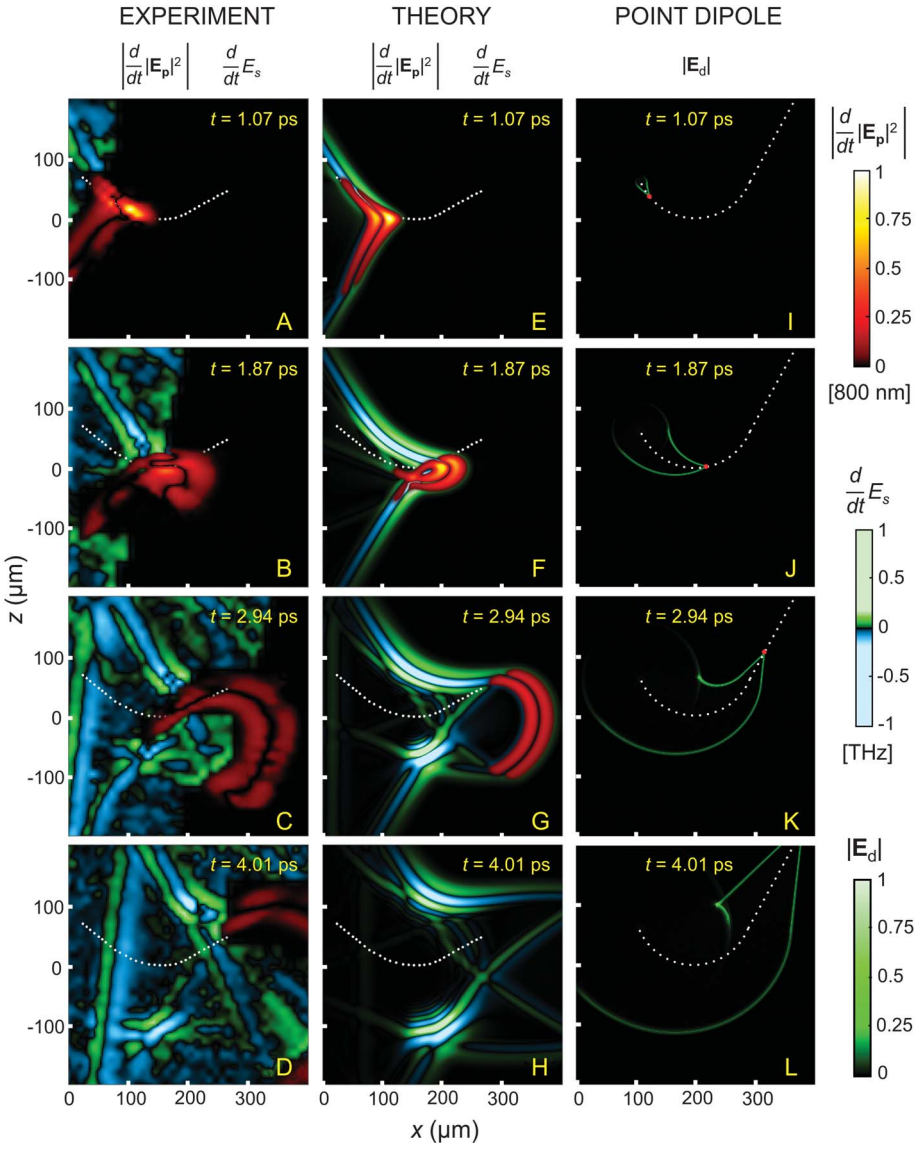

Fig. 4. Synchrotron radiation from a superluminal accelerating pulse. (**A** to **D**) Two-dimensional plots showing results of the orthogonal pump-probe measurements. The signal proportional to the time-derivatives of the pump intensity $|\mathbf{E}_P|^2$ and that of the terahertz field, E_S, were isolated and plotted on separate scales. (**E** to **H**) Theoretical $|d|\mathbf{E}_P|^2/dt|$ and dE_S/dt. The dashed white curve is the trajectory derived from calculations of the pump intensity. (**I** to **L**) Radiation emitted by a point dipole with speed 2.86 times faster than that of light (this value is the ratio between the zero-frequency refractive index of $LiTaO_3$ and the group index at 800 nm). The dipole, indicated by the red dot, propagates first along a circular arc subtended by an angle of $3\pi/4$ and then follows a linear path for $t > 2.6$ ps. The origin of time and the parameters of the dipole trajectory were chosen to provide a good qualitative comparison with the pulse propagation data; the dipole emission associated with the linear part of the motion simulates that of the pump pulse upon its diffraction at $t \gtrsim 2.94$ ps. The pulse emission patterns at $t = 1.07$ closely resemble that of conventional Cherenkov radiation. The observation of two Cherenkov-related curved branches, prominently observed for $t \geq 1.87$ ps in all panels, as well as the cusp in the inner radiation branch at $t = 2.94$ and 4.01 ps, are features characteristic of superluminal synchrotron radiation.

radiation. Specifically, both the theoretical and measured terahertz fields show the presence of two (inner and outer) radiation branches as opposed to a single one (*28*). As the early time panels A and E show, these branches meet in a form that strongly resembles the characteristic shock wave of Cherenkov radiation. By the time the pulse passes through the midpoint of the circular trajectory, the fields have developed prominent curvatures in both branches, which are readily apparent for $t \geq 1.87$ ps. Such a distorted, curvilinear Cherenkov pattern is also evident in the single-dipole results. Another key feature of superluminal speeds is the formation of a cusp in the inner radiation branch (*34*, *35*), which is clearly observed in the calculations for the single dipole. Note that the cusp is well developed by the time the dipole makes one-half of a revolution. The 800-nm pulse in the experiment completes between one-quarter and one-half of a revolution. Consistent with the single-dipole data, the motion of our pulses produces a small cusp in the inner radiation branch that can be seen in Fig. 4 at $t = 2.94$ ps near $(x, z) = (175\ \mu m, 75\ \mu m)$ and at $t = 4.01$ ps near $(x, z) = (200\ \mu m, 100\ \mu m)$.

REFERENCES AND NOTES

1. F. R. Elder, A. M. Gurewitsch, R. V. Langmuir, H. C. Pollock, *Phys. Rev.* **71**, 829–830 (1947).
2. D. Iwanenko, I. Pomeranchuk, *Phys. Rev.* **65**, 343 (1944).
3. J. P. Blewett, *Phys. Rev.* **69**, 87–95 (1946).
4. J. P. Blewett, *J. Synchrotron Radiat.* **5**, 135–139 (1998).
5. A. Ardavan *et al.*, *J. Appl. Phys.* **96**, 4614 (2004); **96**, 7760(E) (2004).
6. V. L. Ginzburg, S. I. Syrovatskii, *Annu. Rev. Astron. Astrophys.* **3**, 297–350 (1965).
7. G. A. Siviloglou, D. N. Christodoulides, *Opt. Lett.* **32**, 979–981 (2007).
8. G. A. Siviloglou, J. Broky, A. Dogariu, D. N. Christodoulides, *Phys. Rev. Lett.* **99**, 213901 (2007).
9. I. Kaminer, R. Bekenstein, J. Nemirovsky, M. Segev, *Phys. Rev. Lett.* **108**, 163901 (2012).
10. P. Zhang *et al.*, *Opt. Lett.* **37**, 2820–2822 (2012).
11. F. Courvoisier *et al.*, *Opt. Lett.* **37**, 1736–1738 (2012).
12. Y. Hu *et al.*, *Sci. Rep.* **7**, 8695 (2017).
13. I. Dolev, I. Kaminer, A. Shapira, M. Segev, A. Arie, *Phys. Rev. Lett.* **108**, 113903 (2012).
14. P. Polynkin, M. Kolesik, J. V. Moloney, G. A. Siviloglou, D. N. Christodoulides, *Science* **324**, 229–232 (2009).
15. R. Merlin, *Science* **317**, 927–929 (2007).
16. A. Grbic, L. Jiang, R. Merlin, *Science* **320**, 511–513 (2008).
17. N. Yu *et al.*, *Science* **334**, 333–337 (2011).
18. X. Ni, N. K. Emani, A. V. Kildishev, A. Boltasseva, V. M. Shalaev, *Science* **335**, 427 (2012).
19. D. Lin, P. Fan, E. Hasman, M. L. Brongersma, *Science* **345**, 298–302 (2014).
20. R. C. Devlin, M. Khorasaninejad, W. T. Chen, J. Oh, F. Capasso, *Proc. Natl. Acad. Sci. U.S.A.* **113**, 10473–10478 (2016).
21. I. Kaminer, J. Nemirovsky, M. Rechtsman, R. Bekenstein, M. Segev, *Nat. Phys.* **11**, 261–267 (2015).
22. A. S. Barker Jr., A. A. Ballman, J. A. Ditzenberger, *Phys. Rev. B* **2**, 4233–4239 (1970).
23. V. L. Ginzburg, *Phys. Usp.* (Engl. transl.) **39**, 973 (1996). [translation from *Usp. Fiziol. Nauk* **166**, 1033 (1996)].
24. V. L. Ginzburg, V. Ya. Éĭdman, *Sov. Phys. JETP* **36**, 1300 (1959).
25. G. N. Afanasiev, *Vavilov-Cherenkov and Synchrotron Radiation: Foundations and Applications* (Kluwer, 2005).
26. V. P. Zrelov, in *Cherenkov Radiation in High-Energy Physics* (Israel Program for Scientific Translations, 1970), p. 31.
27. J. K. Wahlstrand, R. Merlin, *Phys. Rev. B* **68**, 054301 (2003).
28. J. D. Jackson, in *Classical Electrodynamics* (Wiley, ed. 3, 1999), chap. 14.
29. T. Wulle, S. Herminghaus, *Phys. Rev. Lett.* **70**, 1401–1404 (1993).
30. E. Greenfield, M. Segev, W. Walasik, O. Raz, *Phys. Rev. Lett.* **106**, 213902 (2011).
31. M. Henstridge *et al.*, *Optica* **5**, 678 (2018).
32. Materials, methods, and supplemenatry media are available online.
33. T. E. Stevens, J. K. Wahlstrand, J. Kuhl, R. Merlin, *Science* **291**, 627–630 (2001).
34. B. M. Bolotovskiĭ, V. P. Bykov, *Sov. Phys. Usp.* (Engl. transl.) **33**, 477 (1990). [translation from *Usp. Fiziol. Nauk* **160**, 141 (1990)].
35. H. Ardavan, A. Ardavan, J. Singleton, *J. Opt. Soc. Am. A* **20**, 2137–2155 (2003).

ACKNOWLEDGMENTS

Funding: This work was supported by the MRSEC Program of the National Science Foundation under grant DMR-1120923 and the Air Force Office of Scientific Research under MURI grant FA9550-14-1-0389. The $LiTaO_3$ substrates were prepared at the Lurie Nanofabrication Facility, University of Michigan, and the metasurface was fabricated at the Birck Nanotechnology Center, Purdue University. **Author contributions:** R.M. conceived and

supervised the project; M.H. designed and carried out the ultrafast optical measurements, performed the calculations, and prepared the $LiTaO_3$ substrates; C.P. designed the metasurface with input from A.G.; D.W. fabricated the metasurface with contributions from V.M.S. and A.B.; and M.H. wrote the manuscript with help from R.M. All authors reviewed and commented on the manuscript. **Competing interests:** We declare no competing interests. **Data and materials availability:** All data are presented in the manuscript and supplementary materials.

SUPPLEMENTARY MATERIALS

www.sciencemag.org/content/362/6413/439/suppl/DC1
Materials and Methods
Supplementary Text
Fig. S1
Movie S1
References (*36*–*38*)

14 March 2018; accepted 30 August 2018
10.1126/science.aat5915